nature communications

Article

https://doi.org/10.1038/s41467-025-67644-1

Accelerated land surface greening caused by earlier permafrost thawing

Received: 13 January 2025

Accepted: 4 December 2025

Published online: 16 December 2025

Check for updates

Hao Hua[1,2,7], Jian Wang[1,2,7], Constantin M. Zohner[3], Josep Peñuelas[4,5], Youhua Ran[6] & Chaoyang Wu[1,2]

Persistent and above-average warming has advanced the start of spring permafrost thawing, intensifying climate warming through carbon feedbacks. However, the extent to which variations in spring permafrost thawing contribute to greening trends in permafrost-affected areas (i.e., increases in vegetation greenness) over time remains unclear, limiting our understanding of the ecological consequences of permafrost degradation. Analyzing 40-year freeze/thaw data and multiple satellite-derived greenness indicators, we identify widespread increases in the sensitivity of spring greenness to spring permafrost thawing based on moving-window analyses, indicating that advances in spring permafrost thawing have played a progressively stronger role in promoting spring greening, particularly in boreal forests and tundra regions underlain by continuous permafrost. In addition to the region-specific climate and permafrost conditions, we uncover biogeophysical pathways accounting for the increase in sensitivity of spring greenness to spring permafrost thawing, including reduced albedo, earlier vegetation phenology, and enhanced soil moisture infiltration. Notably, state-of-the-art Dynamic Global Vegetation Models consistently underestimate both the magnitude and variability of sensitivity of spring greenness to spring permafrost thawing. These findings highlight the temporal changes in vegetation responses to freeze-thaw dynamics, necessitating improved model projections concurrent with climate change.

Permafrost regions, which cover ~25% of the Northern Hemisphere, are undergoing substantial greening over recent decades due to warming temperatures, manifested as increased vegetation greenness, biomass, productivity, and growing season length[1–3]. Greening over permafrost regions profoundly influences carbon cycling and energy fluxes, with far-reaching implications for global climate systems[4–6]. Concurrently, persistent and above-average warming has accelerated permafrost degradation, contributing to positive climate feedback through enhanced soil carbon release (i.e., permafrost carbon feedback)[7]. This degradation also affects vegetation dynamics by altering regional energy and water balance[8,9], hydrothermal properties of the soil[10,11], and nutrient mineralization[12,13]. Despite these advances, the relationship between permafrost changes and greening remains poorly understood, partly due to a research focus on soil warming and deepening active layers, which often overlooks the timing of freeze-thaw cycles—an essential indicator of permafrost-climate interactions[13].

Warming-induced advances in the start of spring permafrost thawing (SOT) have been documented through ground-based

[1]The Key Laboratory of Land Surface Pattern and Simulation, Institute of Geographical Sciences and Natural Resources Research, Chinese Academy of Sciences, Beijing, China. [2]University of the Chinese Academy of Sciences, Beijing, China. [3]Department of Environmental Systems Science, Institute of Integrative Biology, ETH, Zurich, Zurich, Switzerland. [4]CSIC, Global Ecology Unit CREAF-CSIC-UAB, Barcelona, Catalonia, Spain. [5]CREAF, Barcelona, Catalonia, Spain. [6]Northwest Institute of Eco-Environment and Resources, Chinese Academy of Sciences, Lanzhou, China. [7]These authors contributed equally: Hao Hua, Jian Wang. e-mail: wucy@igsnrr.ac.cn

measurements[14] and satellite observations[15,16], revealing consistent trends but varying magnitudes. Here, SOT refers to the timing when the seasonally frozen active layer above permafrost begins to thaw, serving as a key indicator of land surface changes and permafrost feedback mechanisms[17]. Acting as an aquitard, permafrost retains soil moisture near plant roots, supporting nutrient cycles essential for plant growth and productivity[18]. Consequently, an earlier SOT may facilitate vertical and horizontal soil water movement, enhancing root-level water and nutrient availability, and promoting spring greening through earlier green-up dates (GUD) and increased leaf area[12,16]. However, under warming and drying conditions, earlier SOT has also caused surface soil drying and nutrient depletion, irreversibly accelerating desertification in alpine ecosystems such as the Qinghai-Tibet Plateau[19]. In addition to the spatially non-uniform responses of vegetation growth to SOT changes, the impacts of SOT are likely to be temporally non-stationary due to rapid anthropogenic climate change and vegetation acclimation[20,21]. Climate warming may destabilize the interactive relationship between permafrost and vegetation by altering landscapes and soil hydrology[13,22]. Permafrost greening cannot be fully explained by climate warming alone; soil and hydrological changes associated with permafrost dynamics are also critical contributors[21,23–26], highlighting the urgent need to investigate the role of SOT shifts in shaping vegetation trends over time.

To address this, we quantify changes in the sensitivity of spring greenness to SOT (β_{SOT}) from 1982 to 2021 for different permafrost and vegetation types over permafrost regions in the northern hemisphere (Supplementary Fig. 1) using a moving window approach. By integrating daily freeze/thaw data, satellite-derived greenness metrics, and a suite of environmental variables (Methods; Supplementary Table 1 and 2), we confirm the advancements in SOT and permafrost greening trends in spring (Supplementary Figs. 2 and 3), identify regions with increased and decreased β_{SOT}, and explore the mechanisms driving these variations. Employing machine learning techniques, causal inference analyses, and structural equation models, we analyze the temporal variability of β_{SOT}, identify the spatial patterns and environmental pathways contributing to these changes, and assess the ability of Dynamic Global Vegetation Models (DGVMs) to replicate the observed trends (Methods; Supplementary Fig. 4).

Results

Increasing sensitivity of spring greenness to SOT

Advances in SOT were significantly associated with increased spring greenness (April to June) across different vegetation types in Northern permafrost regions during 1982–2021. Based on ridge regression, the estimated sensitivities (β_{SOT}) were predominantly positive, with spatially averaged values of 14.8, 2.4, and 3.6 ‰ day^{-1} for kernel normalized difference vegetation index (kNDVI), solar-induced chlorophyll fluorescence (SIF), and gross primary productivity (GPP), respectively (Supplementary Fig. 5), suggesting that earlier thawing tends to correspond with enhanced spring vegetation activity. Some regions also exhibited negative β_{SOT}, possibly reflecting locally constrained responses to earlier thawing. We then determined the time series of β_{SOT} using 15-year moving windows from 1982 to 2021 at each pixel and found that 38.6% of regions exhibited a significant increase in β_{SOT} for kNDVI, while 22.0% showed a decreasing trend ($p < 0.05$) (Fig. 1A). Comparable patterns were found for SIF (38.2% increase; 24.4% decrease, Fig. 1D) and GPP (44.8% increase; 17.3% decrease, Fig. 1G). The strongest increasing trends in β_{SOT} were concentrated in continuous permafrost regions, and diminished with decreasing permafrost continuity (Supplementary Fig. 6). Temporal changes in spatially averaged β_{SOT} confirmed significant increasing trends, with slopes of 0.70, 0.17, and 0.35 ‰ day^{-1} window^{-1} for kNDVI, SIF, and GPP (Fig. 1B, E, H). By vegetation type, Boreal Forests and Tundra regions exhibited the most pronounced increases in β_{SOT}, consistent across kNDVI, SIF, and GPP (Fig. 1C, F, I). To test the robustness of these results, we performed additional analyses using alternative moving window sizes and several other greenness indicators from complementary datasets beyond those presented in the main text. The results remained consistent, differing only in magnitude (Methods; Supplementary Fig. 7). In addition, a spatial consistency analysis across six greenness datasets showed that 77.2% of pixels exhibited consistent directional responses, further supporting our findings (Supplementary Fig. 8). As another validation, we applied a log-log regression to account for possible nonlinear SOT-greenness relationships, alongside a standard multiple linear regression for comparison (Methods). Both approaches consistently confirmed the widespread increases in β_{SOT} (Supplementary Fig. 9). Taken together, these robustness checks demonstrate an increasing and stimulating impact of SOT on permafrost vegetation greening in spring over the past four decades.

Spatial attribution analysis of β_{SOT} trends

We quantified the contributions of permafrost, climate, hydrology, vegetation and soil nutrition factors in explaining the spatial variability of β_{SOT} trends, using a random forest (RF) algorithm combined with SHapley Additive exPlanations (SHAP) values (Methods), with β_{SOT} trend derived from ridge regression based on kNDVI as a representative indicator. The RF model explained, on average, 81% of the spatial variability in β_{SOT} trends ($R^2 = 0.81$) (Fig. 2G). Among the environmental factors, mean SOT, mean temperature, and temperature trend had strong association in β_{SOT} trends, emphasizing the combined influence of baseline thaw timing and climate warming in driving spatial variations in β_{SOT} trends (Fig. 2H). Grouping pixels into different vegetation types overall confirms the importance of background permafrost and climate conditions in accounting for the spatial patterns of β_{SOT} trends (Supplementary Fig. 10). The six most important environmental factors, ranked by their absolute SHAP values, were selected to explore regional differences in β_{SOT} trends. Comparing regions with increased and decreased β_{SOT}, we found distinct differences in these environmental characteristics. For permafrost factors, regions with decreased β_{SOT} experienced earlier thawing by ~10.7 days (Fig. 2A) and later freezing by about 6.9 days (Fig. 2D) compared to regions with increased β_{SOT}. These results suggest that in severely degraded permafrost regions with extended non-frozen periods, vegetation shows weaker sensitivity to thaw timing, as reflected by attenuated β_{SOT}. For climatic factors, regions with increased β_{SOT} exhibited faster warming rates (0.02 °C year^{-1}), despite having mean temperatures that were 2.04 °C lower than decreased β_{SOT} regions (Fig. 2B, C). Lower shortwave radiation in increased regions (2.2 W m^{-2} less on average, Fig. 2F) suggests greater reliance on non-radiative energy inputs enabled by earlier thawing to meet vegetation energy demands. Greening trends also influenced β_{SOT} trends, with regions of increased β_{SOT} characterized by slower greening rates (Fig. 2E), suggesting that inherent vegetation characteristics may modulate the sensitivity of greenness to thaw timing.

Biogeophysical processes mediating the SOT-greenness relationship

While the spatial patterns of divergent β_{SOT} trends are relatively well characterized, understanding the mechanisms driving their temporal evolution at a given location remains more challenging. We hypothesized that the temporal changes in β_{SOT} are mediated by (i) energy balance processes through changes in albedo, (ii) phenological dynamics through shifts in GUD, and (iii) water supply through variations in soil moisture and runoff. To test these hypotheses, we applied causal inference and partial correlation analyses to examine how variations in SOT propagate through intermediate processes, i.e., albedo, GUD, and the difference between root-zone and surface soil moisture (ΔSM), that mediate its influence on spring greenness. We then used

https://doi.org/10.1038/s41467-025-67644-1

structural equation modeling (SEM) to quantify the individual and combined contributions of these mediating factors during two separate periods (1982–2001 and 2002–2021).

Using a causal inference analysis (i.e., convergent cross mapping, or CCM) for the entire period (1982–2021), we identified significant causal links between β_{SOT} and albedo, GUD, and ΔSM (Fig. 3A–C). The overall CCM results, represented by the red lines, confirmed causality for all three variables, with Spearman correlation coefficients (rho, Methods) reaching 1 ($p = 0.00$). GUD exhibited the highest proportion of pixels with causality (65.9%), followed by albedo (65.6%) and ΔSM (65.3%). Partial correlation analyses for the two periods revealed that the roles of albedo, GUD, and ΔSM as intermediaries linking SOT to greenness differed between 1982–2001 and 2002–2021 (Fig. 3D–F). SOT-albedo correlations were consistently positive in both periods (~33%) but showed a shift in albedo-kNDVI relationships for two periods, with significantly negative correlations increasing from 48% to 54.5% ($p < 0.05$), indicating a growing negative mediation by albedo in recent decades. GUD maintained stable positive correlations with SOT (~12%) but exhibited a significant increase in negative correlations with greenness, rising from 13.1% to 25.6%, reflecting its intensified role in modulating spring greenness. ΔSM consistently showed negative correlations with SOT (~11%) but experienced a notable rise in positive correlations with kNDVI, from 4.9% to 8.9%, underscoring its increasing importance in supporting vegetation water demands. SEM analyses

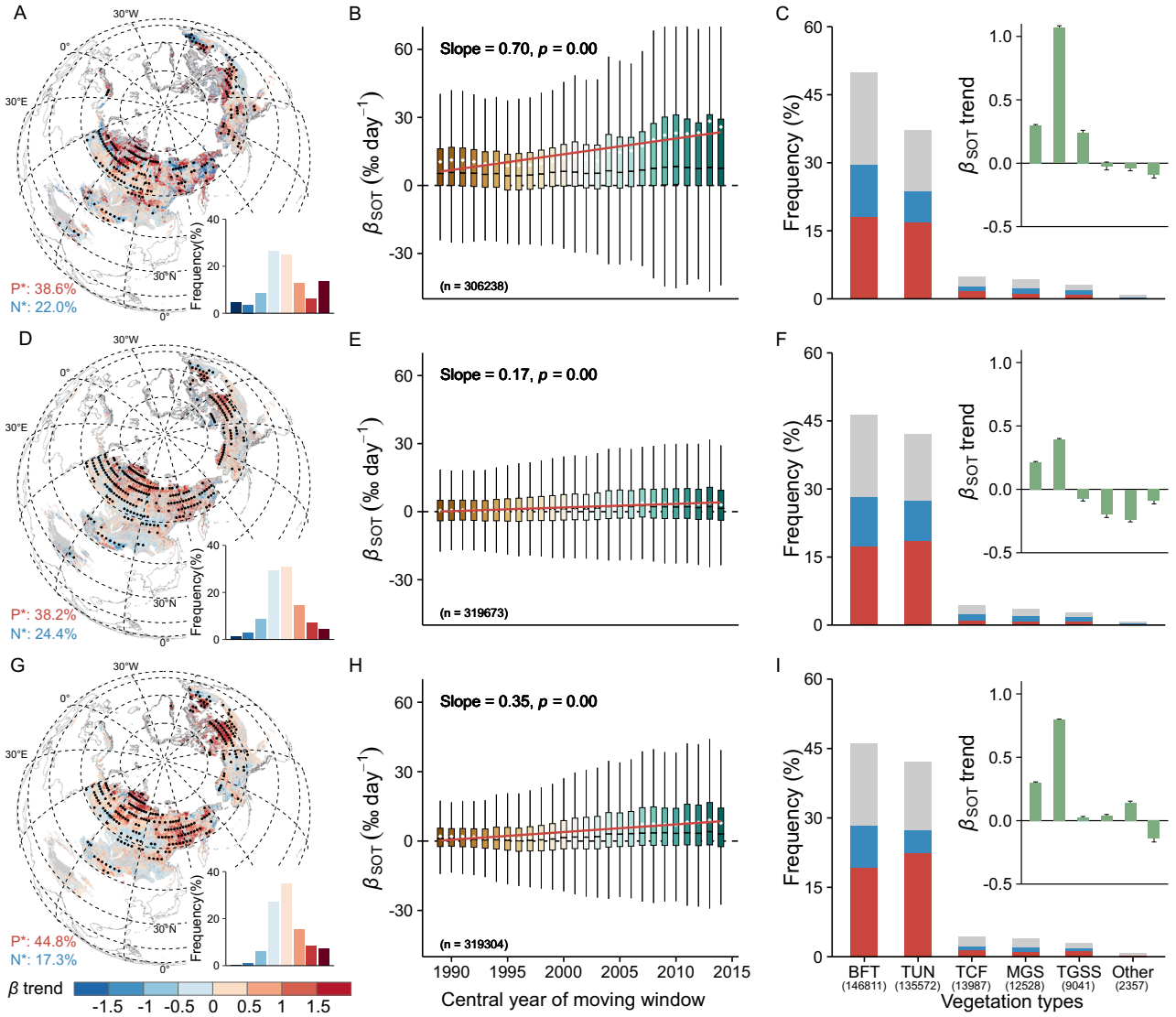

Fig. 1 | Temporal changes in β_{SOT}. Spatial distribution of the trend of β_{SOT} estimated from kNDVI (**A**), SIF (**D**), and GPP (**G**). P* and N* indicate the percentage of significantly positive and negative trends, respectively ($p < 0.05$). Temporal changes in spatially averaged β_{SOT} using a 15-year moving window for kNDVI (**B**), SIF (**E**), and GPP (**H**). Box plots show medians (center lines), interquartile ranges (boxes), and whiskers extending to 1.5×IQR; white points indicate means. The red line represents the linear regression based on the mean of each box, and the slope denotes the rate of change in β_{SOT} per moving window (‰ day^{-1} window^{-1}). The numbers in brackets represent the number of pixels (n). Trends were estimated using the Theil–Sen slope, and their significance was assessed with the two-sided Mann–Kendall test ($p < 0.05$). Distribution of β_{SOT} trends across different vegetation types for kNDVI (**C**), SIF (**F**), and GPP (**I**). Red bars indicate significantly positive trends, blue bars indicate significantly negative trends, and grey bars represent non-significant trends. Insets show the mean trend of β_{SOT} for each vegetation type, with error bars representing the 95% confidence intervals. Vegetation type abbreviations are: BFT, Boreal Forests/Taiga; TUN, Tundra; TCF, Temperate Conifer Forests; MGS, Montane Grasslands and Shrublands; TGSS, Temperate Grasslands, Savannas & Shrublands; Other, including Temperate Broadleaf & Mixed Forest and Flooded Grasslands and Savannas (Supplementary Table 3). The numbers in brackets represent the number of pixels (**I**). Source data are provided as a Source Data file.

https://doi.org/10.1038/s41467-025-67644-1

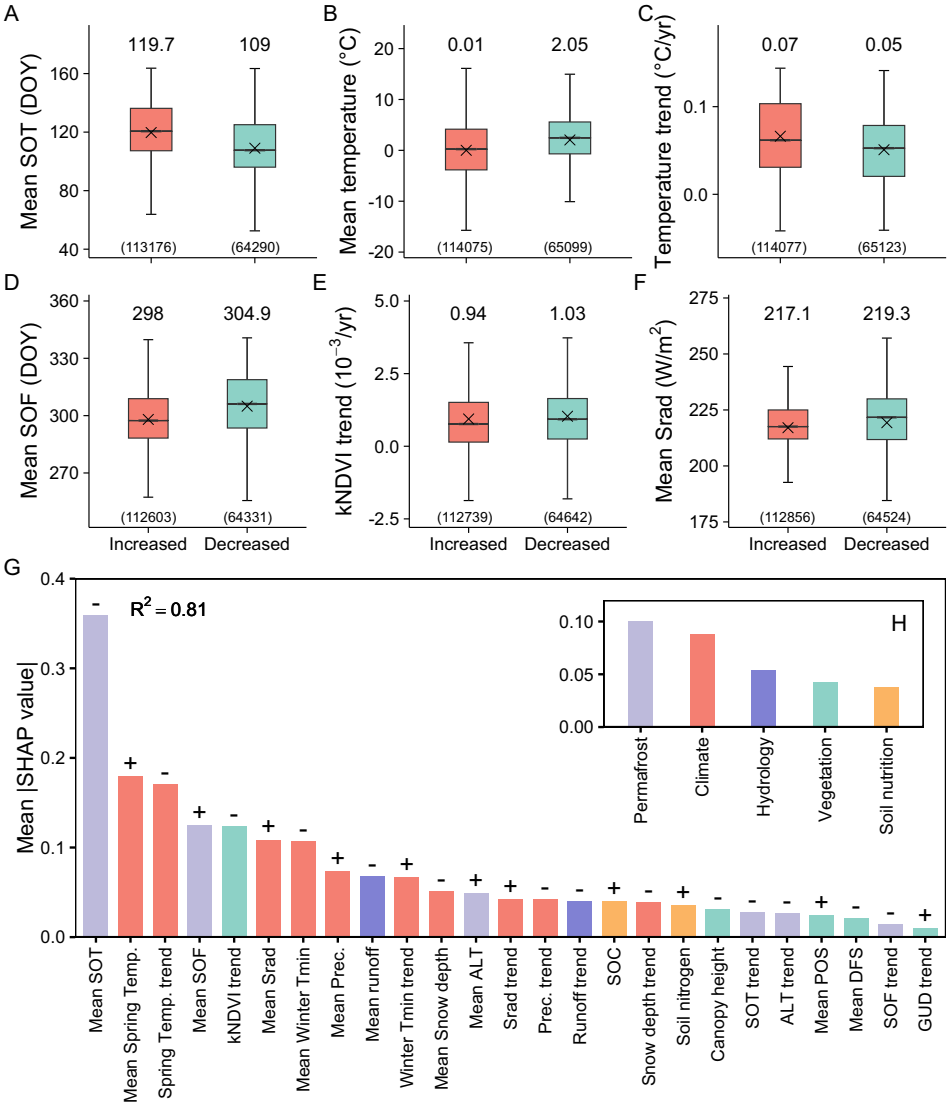

Fig. 2 | Driving factors for the spatial distribution of trends in β_{SOT}. Grouped bar plots of six key environmental factors, i.e., Mean SOT (**A**), mean temperature (**B**), temperature trend (**C**), mean start of autumn permafrost frozen (SOF) (**D**), kNDVI trend (**E**), and mean shortwave radiation (Srad) (**F**), across regions with increased and decreased β_{SOT} trends. Box plots show medians (center lines), interquartile ranges (boxes), and whiskers extending to 1.5×IQR; crosses indicate means. The numbers in brackets represent the number of pixels. **G** The relative importance of environmental factors controlling the spatial variability of trends in β_{SOT}, determined by a random forest model using mean absolute SHAP values. The six most important variables, ranked highest in importance, correspond to (**A**–**F**). **H** All factors were aggregated into five categories: permafrost, climate, hydrology, vegetation and soil nutrition, for comparison of their relative importance (Methods). Tmin minimum air temperature, ALT active layer thickness, SOC soil organic carbon, POS peak of growing season; DFS, the autumn date of foliar senescence. Source data are provided as a Source Data file.

overall confirmed divergent regulations of SOT on greenness via albedo, GUD, and ΔSM for two periods (Fig. 3G–I). For regions with decreasing β_{SOT}, we found that shrub-dominated biomes with deeper root systems tended to experience more negative ΔSM trends (Supplementary Fig. 11), suggesting that early thaw may limit water accessibility in deeper soil layers, thereby weakening the vegetation response to SOT.

Evaluation of DGVM performance in reproducing β_{SOT} trends

We further tested whether current state-of-the-art ecosystem models can reproduce the observed increasing β_{SOT}. Using the 16-model ensemble mean vegetation productivity from the "Trends and drivers of the regional scale terrestrial sources and sinks of carbon dioxide" (TRENDY) project, we found that the proportions of regions with significantly increased (32.2%) and decreased (28.8%) β_{SOT} were comparable, indicating no clear spatial dominance in trend direction (Fig. 4A). The models predicted an overall increase in β_{SOT} based on the moving-window approach (slope = 0.09‰ day^{-1} window^{-1}, $p = 0.00$, Supplementary Fig. 12), but the magnitude of the increase was 87.1% weaker than the observed results of kNDVI. The high standard deviation of β_{SOT} among models, particularly in the continuous permafrost zone (Fig. 4B), highlights substantial inconsistencies in model simulations for permafrost regions. Analysis of individual model outputs showed that, with the exception of ORCHIDEE (Organizing Carbon and Hydrology in Dynamic Ecosystems) and YIBs (Yale Interactive Terrestrial Biosphere), most TRENDY models did not fully capture the increase-dominant trends in β_{SOT} (Fig. 4C). Spatial consistency analysis at pixel level revealed that approximately half of the simulated trends differed from observations (Fig. 4D), reflecting variability and limitation in model projections across regions.

https://doi.org/10.1038/s41467-025-67644-1

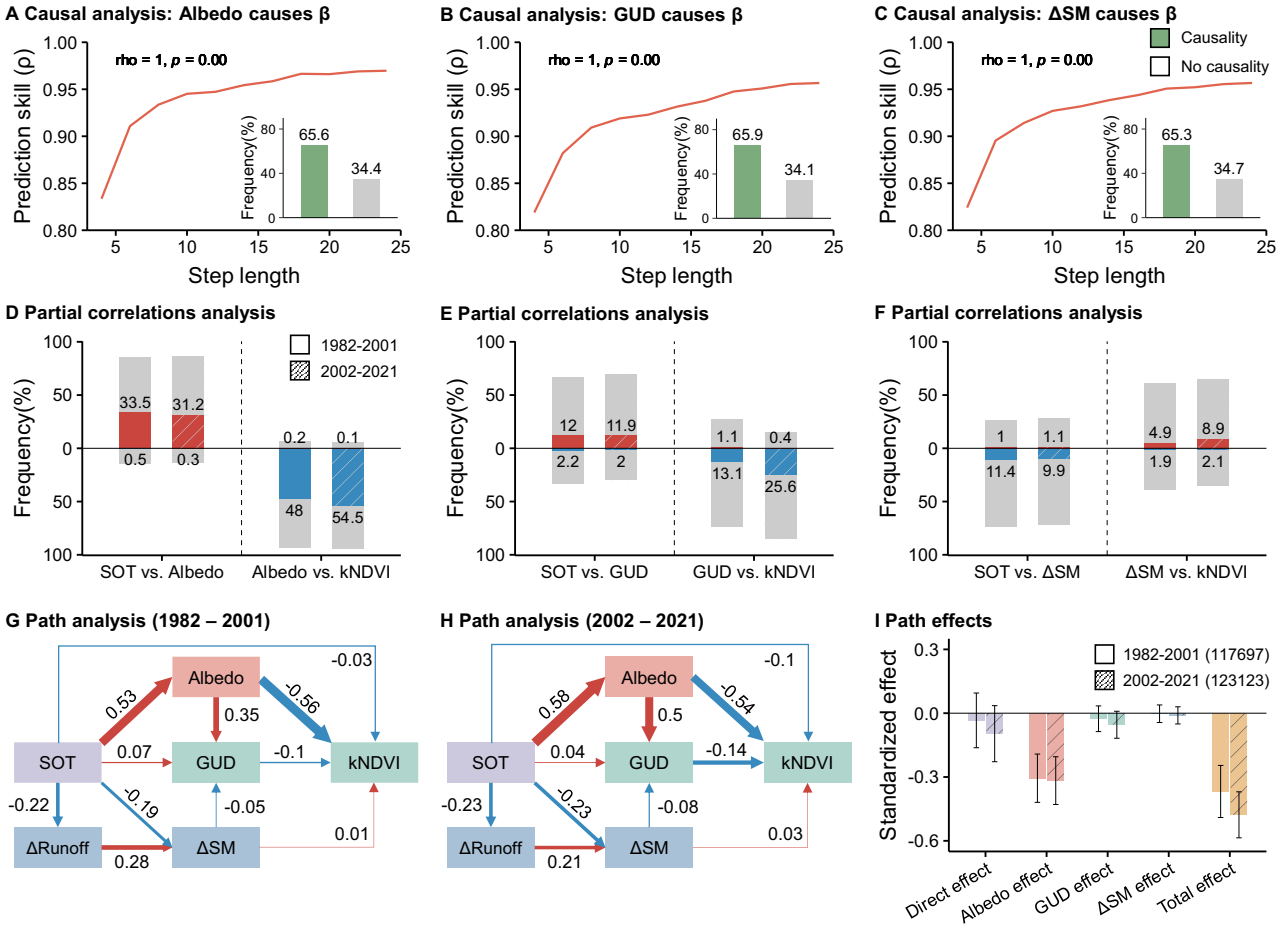

Fig. 3 | Underlying mechanisms driving trends in β_{SOT}. Causal analysis of albedo (**A**), GUD (**B**), and ΔSM (**C**) as drivers of β_{SOT} changes. CCM was used to establish causal links, with causality confirmed when the predictive skill (ρ) converges with step length. The significance of convergence was determined using a two-sided Spearman's rank correlation test ($p < 0.05$). Red lines represent overall CCM results based on spatially averaged β_{SOT}, and maps show spatial distributions of causality. Partial correlation analysis showing the role of albedo (**D**), GUD (**E**), and ΔSM (**F**) as intermediaries linking SOT and kNDVI, excluding the effects of climate change and CO_2 concentrations. SEM illustrates path relationships between SOT and kNDVI for 1982–2001 (**G**) and 2002–2021 (**H**). Numbers indicate the mean standardized path coefficients, with blue and red arrows representing negative and positive effects, respectively. Arrow widths reflect the magnitudes of the coefficients. **I**, Direct, intermediary (albedo, GUD, and ΔSM), and total effects of SOT on kNDVI across the two periods. Data are presented as mean ± 0.5 SD. The numbers in brackets represent the number of pixels. Source data are provided as a Source Data file.

Discussion

The synergistic relationship between permafrost and vegetation plays a crucial role in regulating regional carbon fluxes but is increasingly destabilized by rapid permafrost degradation[7]. Warming accelerates soil carbon release while promoting vegetation growth, creating a dynamic feedback system that is highly sensitive to the timing of freeze-thaw cycles[17,27]. Our findings indicate widespread increases in β_{SOT}, with regions exhibiting enhanced sensitivity of vegetation greenness to SOT outnumbering those with weakened sensitivity (Fig. 1). Interestingly, the weakened sensitivity was primarily observed in shrub-dominated regions, where deeper-rooted vegetation may face limited water access in early spring due to still-frozen or poorly drained deep soils, thereby constraining their response to earlier thawing (Supplementary Fig. 11). While extant studies have underscored the critical role of freeze-thaw dynamics in shaping Arctic ecosystems[1,13], this study provides the direct evidence of the temporal evolution of β_{SOT}, highlighting the growing dependence of vegetation on the timing of freeze-thaw cycles.

We identified the spatial drivers of β_{SOT} trends, confirming the critical roles of background climate, soil thermal and hydrological processes, and vegetation traits in shaping the SOT-greenness relationship (Fig. 2). From a temporal perspective, our mechanistic analyses revealed three dominant pathways, i.e., energy absorption (reduced albedo), vegetation dynamics (advanced GUD), and water supply (enhanced vertical soil moisture infiltration), that collectively explain the observed increases in β_{SOT} (Fig. 3). Reduced albedo, a well-documented consequence of earlier greening[26,28], enhances surface energy absorption, which subsequently promotes vegetation growth. This effect has intensified over time, as shown by the stronger negative correlation between albedo and greenness in recent decades (Fig. 3D). Earlier GUD extends the growing season (Fig. 3E), providing plants with additional time for carbon assimilation and biomass accumulation in spring[25,29,30]. Additionally, shifts from surface runoff to subsurface infiltration have improved soil water availability[31], supporting vegetation growth under earlier thawing conditions[16,17]. We observed a notable temporal shift in the relative contributions of these pathways across two distinct periods. Although our statistical analysis treated SOT as an exogenous driver preceding spring mean albedo, potential feedbacks highlight the need to consider coupled energy-vegetation processes increasingly recognized as critical to Arctic ecosystem responses to climate change[4].

Despite the robustness of our observational findings, current terrestrial ecosystem models consistently underestimated both the magnitude and spatial variability of β_{SOT} trends. Model-predicted

https://doi.org/10.1038/s41467-025-67644-1

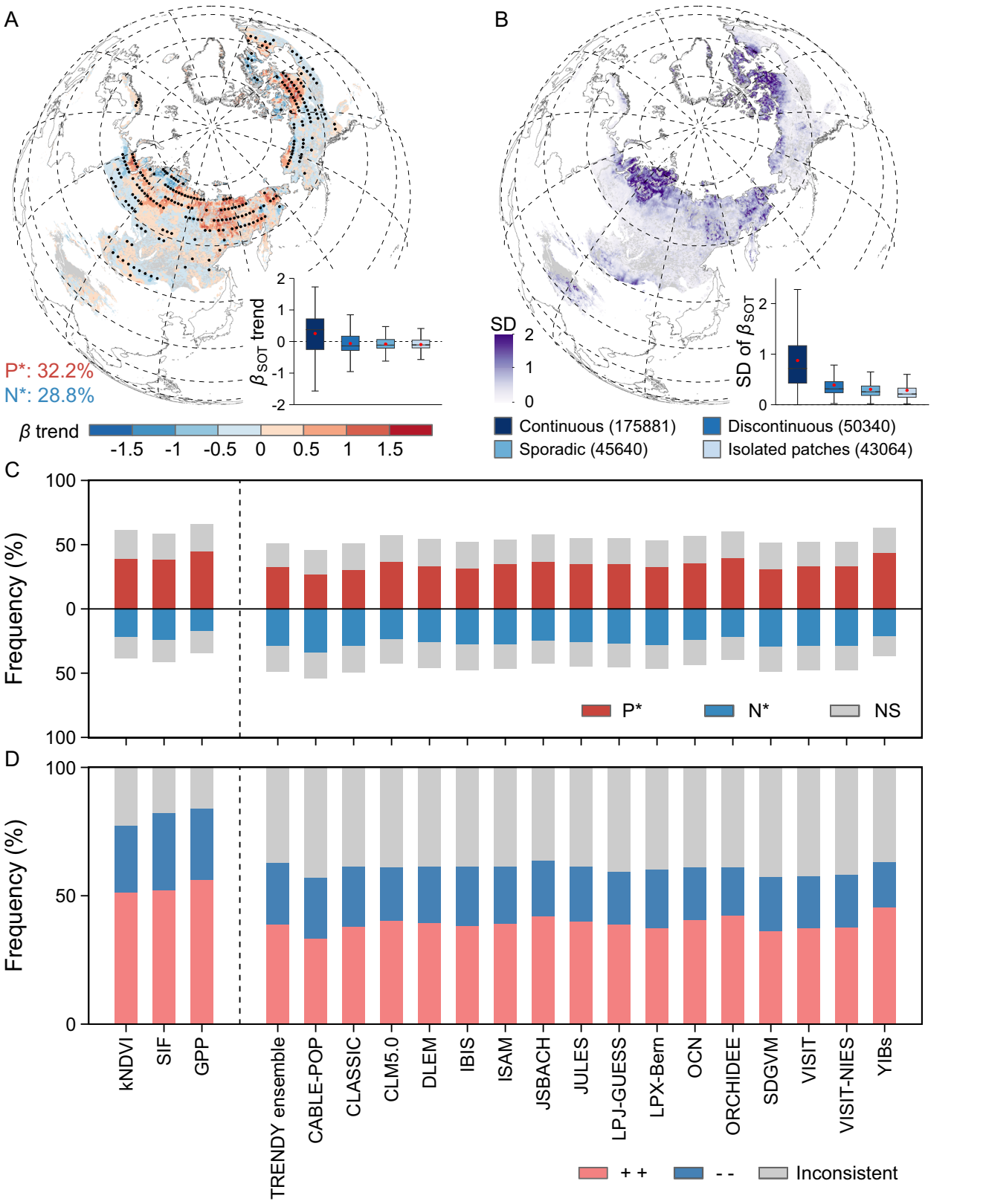

increases in β_{SOT} were 87.1% weaker than observed trends, with particularly poor spatial consistency in continuous permafrost zones (Fig. 4). These discrepancies reflect significant limitations in the representation of freeze-thaw dynamics and their ecological consequences. In particular, the simulation of permafrost-specific hydrological processes, such as the three-phase transitions of water (liquid-ice-vapor) in near-surface soils, remains a critical challenge for improving model realism in high-latitude ecosystems[32]. Although some land surface models (e.g., ISAM) have introduced vertically resolved soil biogeochemistry to better capture subsurface carbon

Fig. 4 | Temporal changes in β_{SOT} simulated by state-of-the-art ecosystem models. A Spatial distribution of the trend of β_{SOT} estimated from an ensemble of state-of-the-art models (Supplementary Table 4), with inset box plots showing trends across permafrost types. **B** Standard deviation (SD) of β_{SOT} among the models, with inset box plots showing SDs across permafrost types. Box plots show medians (center lines), interquartile ranges (boxes), and whiskers extending to 1.5×IQR; red points indicate means. The numbers in brackets represent the number of pixels across permafrost types. **C** Comparison of observed trends in β_{SOT} (kNDVI, SIF, GPP) with modelled trends from the ensemble of models, focusing on the proportions of significant positive (P*), significant negative (N*), and non-significant (NS) trends. **D** Spatial consistency of trends in β_{SOT} using the majority-vote result from kNDVI, SIF and GPP as the observational baseline (Methods).++ and − − indicate agreement on positive and negative trends, respectively. Trends were estimated using the Theil–Sen slope, and their significance was assessed with the two-sided Mann–Kendall test ($p < 0.05$). Source data are provided as a Source Data file.

processes, their predictive capacity remains limited by structural uncertainties and parameterization gaps[33,34]. These limitations impair the ability of current models to reproduce the complex interactions between permafrost thaw and vegetation growth that underlie observed β_{SOT} trends.

To address these limitations, future modeling efforts should prioritize capturing the evolving sensitivity of vegetation to freeze-thaw timing by improving the representation of soil thermal regimes, hydrological processes, and phenological responses. First, most existing DGVMs lack explicit parameterization of active layer dynamics and three-phase water transitions, which are critical for simulating seasonal thaw and associated vegetation responses[1,32]. Integrating vertically resolved soil thermal-hydrological modules that account for phase change energy and ice content can substantially improve the realism of freeze-thaw simulations[17]. Second, abrupt thaw events, such as ice-rich permafrost collapse, remain largely unrepresented in current models despite their outsized impacts on ecosystem structure and carbon release[35–37]. Including such processes is particularly important in regions with high ground ice content, such as the Yedoma domain[38]. Third, vegetation responses to thaw are strongly mediated by microtopography, rooting depth, and associated water redistribution[39–41]. Incorporating these biophysical controls, such as topography-driven soil moisture heterogeneity and vegetation-specific rooting strategies, can improve simulations of moisture-vegetation interactions during thaw transitions. Lastly, hybrid approaches that combine process-based models (e.g., CLM, LPJ-GUESS) with machine learning offer a promising path to better capture nonlinear and spatially heterogeneous vegetation-soil-climate feedbacks[42]. As warming intensifies and hydrological variability increases, improving the structural realism and responsiveness of DGVMs will be essential for accurately projecting permafrost ecosystem trajectories.

While our study integrates multiple long-term datasets to uncover robust patterns, we acknowledge that uncertainties in key data sources, such as microwave-based freeze-thaw retrievals, satellite-derived albedo, and precipitation estimate, may propagate through the β_{SOT} analysis. To minimize these effects, we implemented rigorous quality control, sensitivity tests, and cross-validation using alternative vegetation indices and spatiotemporal resampling strategies (Supplementary Figs. 13 and 14), all of which supported the stability of our main findings. Nevertheless, residual uncertainties remain and may influence the regional attribution of vegetation sensitivity. Reducing such uncertainties will require improved high-latitude in situ monitoring networks, enhanced satellite product validation, and continued efforts in integrating multi-source datasets. These steps are critical for advancing both empirical assessments and the fidelity of process-based models. As the Arctic continues to warm, capturing the coupled responses of vegetation and permafrost with greater precision will be essential for projecting biosphere-climate feedbacks in a changing Earth system.

Methods

Determination of permafrost thawing and frozen dates

We determined the permafrost thawing and frozen dates using three independent datasets (Supplementary Table 1): (1) a microwave-based freeze-thaw Earth system product, (2) a reanalysis-based skin temperature product, and (3) in-situ observations.

The Freeze-Thaw Earth System Data Record (FT-ESDR) provides daily freeze-thaw classifications derived from 37 GHz passive microwave sensors (SMMR, SSM/I, SSMIS) at 25 km resolution[43]. Each grid cell is assigned one of four surface states: frozen (0), thawed (1), transitional (2), or inverse-transitional (3). Quality control steps were applied to remove erroneous signals near open water bodies or complex terrain.

We used the ERA5-Land skin temperature product from the ECMWF ERA5-Land Daily Aggregated dataset[44]. This dataset provides daily aggregates of hourly skin temperature at ~9 km spatial resolution. Each day was classified into frozen (<0 °C), thawed (>0 °C), or transitional (0 °C) states, aligned with the FT-ESDR classification scheme.

We compiled daily surface temperature records from 39 active-layer monitoring sites within the Global Terrestrial Network for Permafrost (GTN-P, https://gtnp.arcticportal.org/), spanning 2001–2021 and representing major permafrost regions (Supplementary Table 5). These site-level data were processed using the same classification thresholds as ERA5-Land to ensure comparability.

For each dataset, we applied a threshold-based moving-window algorithm widely used in freeze-thaw studies[45,46]. Specifically, the start of spring permafrost thawing (SOT) was defined as the first day within a 15-day window in which ≥12 days were classified as thawed or transitional, i.e., indicating the onset of persistent thaw conditions while minimizing the influence of short-term noise. The start of autumn permafrost frozen (SOF) was defined similarly as the first day within a 15-day window in which ≥12 days were frozen, denoting the return of frozen conditions in autumn[47]. Sensitivity tests confirmed that window size slightly altered absolute dates but did not affect interannual variability[16]. The analysis was constrained to the January–June period to capture spring thawing dynamics. To improve robustness, we compared SOT estimates from FT-ESDR and ERA5-Land and found consistent spatio-temporal patterns (Supplementary Fig. 2). Therefore, the averaged SOT and SOF from both sources was used in all analyses. Site-based SOTs from GTN-P were used for validation (Supplementary Fig. 2).

Indicators of spring greenness

Satellite-based greenness indicators. To quantify spring vegetation greenness, we used multiple satellite-based indicators for the permafrost region of the Northern Hemisphere during 1982–2021. As spring phenology in permafrost regions typically begins in mid-April[16], we defined spring as starting from April to June. The indicators include the kernel normalized difference vegetation index (kNDVI), SIF, and GPP, which are widely used as the proxies of vegetation greenness and photosynthetic activity of vegetation[48–50]. We used spring-averaged values to represent vegetation activity from different perspectives and scales. It should be noted that greenness indicators differ in their ecological meaning (e.g., greenness vs. productivity), and while collinearity exists, they are not fully synchronous[5,51,52]. Caution is therefore needed in interpretation.

kNDVI (Eq. 1) is a nonlinear transformation of NDVI that enhances sensitivity to vegetation greenness by reducing soil background noise and mitigating saturation in dense canopies[48]. The NDVI data were

derived from harmonized AVHRR-MODIS observations with sensor calibration, orbital correction, and machine learning-based fusion[53]. LCSPP (Long-term Continuous SIF-informed Photosynthesis Proxy) is a SIF-based proxy for photosynthesis reconstructed by training neural networks on OCO-2 SIF and bias-corrected AVHRR reflectance. It shows high consistency with both satellite SIF and site-level GPP[54,55]. GPP was obtained from BESS v2.0 (the Breathing Earth System Simulator), a satellite-driven model integrating coupled carbon, water, and energy processes. BESS shows strong agreement with FLUXNET data and provides reliable global GPP estimates[56].

$$kNDVI = \tanh(NDVI^2) \quad (1)$$

To enhance robustness, we further incorporated additional greenness-related datasets with shorter temporal coverage, derived from different sensors and/or reconstruction approaches: (1) GOSIF is a global 8-day 0.05° SIF product reconstructed from OCO-2 SIF, MODIS reflectance, and reanalysis data, with strong agreement to FLUXNET GPP across ecosystem[57]. (2) CSIF provides spatially continuous SIF estimates at 4-day 0.05° resolution using neural networks trained on MODIS reflectance and OCO-2 SIF, capturing realistic spatiotemporal photosynthetic dynamics under clear- and all-sky conditions[58]; (3) VOD (VODCA v2) is a harmonized microwave-derived daily 0.25° vegetation optical depth product[59], reflecting canopy water content by integrating multiple sensors and frequencies through the Land Parameter Retrieval Model. All datasets consistently demonstrated an increasing sensitivity of spring greenness to SOT (Supplementary Fig. 7 and 8), confirming that our conclusions are primarily driven by biogeophysical effects rather than potential biases in observational signals. Full details of all datasets are provided in Supplementary Tables 1 and 2.

Process-based model projections. We utilized model-simulated GPP from 16 terrestrial biosphere models provided by the "Trends and drivers of the regional scale terrestrial sources and sinks of carbon dioxide" (TRENDY) project to analyze vegetation sensitivity to SOT (Supplementary Table 4)[60,61]. TRENDY is an ensemble framework that estimates ecosystem carbon dynamics under varying initial forcing conditions. We used outputs from simulation scenario S3, which incorporates temporal changes in land use, climate, and CO_2 concentration, allowing for an integrated assessment of human and climate-driven influences on vegetation. Model outputs, originally at varying spatial resolutions, were re-gridded to 0.1° × 0.1° and aggregated to calculate spring GPP. These simulations were systematically compared with satellite-based observational data to evaluate their ability to capture temporal variability of SOT effects, providing insights for improving model representations of permafrost-vegetation-climate interactions.

To compare spatial consistency of β_{SOT} trends, we established an observational baseline using a majority voting method with three satellite-derived datasets. For each pixel, if two or more datasets indicated an increase (or decrease) in β_{SOT}, the pixel was classified as increasing (or decreasing).

Climatic and ancillary data

To investigate the relationship between SOT and spring greenness, we utilized a comprehensive range of climatic and ancillary datasets spanning 1982–2021. For consistency across analyses, all datasets were re-gridded to a spatial resolution of 0.1° using the bilinear interpolation method.

Climatic data. Monthly climatic data for 1982–2021 were derived from TerraClimate[62], a dataset of monthly climate for global terrestrial surfaces at a spatial resolution of 1/24°. We calculated the average 2-m temperature (Temp), 2-m minimum temperature (Tmin), precipitation (Prec), and shortwave radiation (Srad) from this dataset for spring (April to June). Global averaged marine surface CO_2 was obtained from the Global Monitoring Laboratory (GML) of the National Oceanic and Atmospheric Administration (NOAA). These variables served as controlling factors to analyze the sensitivity of spring greenness to SOT. Further details on the data are provided in Supplementary Table 1.

Hydrological and surface energy data. To analyze hydrological and energy processes linked to SOT, we used ERA5-Land reanalysis data (0.1° × 0.1°)[44], including surface albedo, snow depth, surface runoff, sub-surface runoff, and volumetric soil water. Snow depth during the cold season was averaged from November to April. Surface soil moisture was derived from layer 1 (0–7 cm depth), while sub-surface soil moisture was calculated as the weighted mean of layers 2 (7–28 cm) and 3 (28–100 cm)[63]. The vertical soil moisture difference (ΔSM) was defined as sub-surface soil moisture minus surface soil moisture, representing vertical gradients. Similarly, the vertical runoff difference (ΔRunoff) was calculated as sub-surface runoff minus surface runoff to capture vertical hydrological dynamics.

Vegetation phenology and structure data. Vegetation phenology, including spring GUD, peak of season (POS), and date of foliar senescence (DFS) during 1982–2021, was derived from the GIMMS NDVI3g+ dataset[64]. Pixels with annual NDVI values below 0.1 were excluded to eliminate sparsely vegetated areas[65], and the NDVI time series was smoothed using a Savitzky-Golay filter[66]. GUD and DFS were estimated as the average of two widely used methods to reduce uncertainty: (1) a dynamic-threshold method, where GUD (or DFS) was defined as the date when the scaled NDVI ratio crossed 0.5 during the spring (or autumn) transition; (2) a double-logistic fitting method, where GUD and DFS corresponded to the date of maximum (or minimum) rate of NDVI change[67,68]. POS was defined as the day when NDVI reached its annual maximum during the summer growing season[69]. The maximum root length at a grid of 0.0083° was obtained from the EartH2Observe[70]. Canopy height data were obtained from the ETH Global Canopy Height 2020 product[71], which integrates Global Ecosystem Dynamics Investigation (GEDI) and Sentinel-2 observations to provide a global canopy height estimate at a 10 m spatial resolution.

Soil attribute data. Active Layer Thickness (ALT) data were obtained from the Permafrost Climate Research Data Package provided by the ESA CCI Permafrost project (1997–2021; 1 km resolution), derived from a thermal model constrained by satellite observations[72]. Additionally, Soil nutrients, including soil organic carbon (SOC) and nitrogen, were sourced from SoilGrids, a global dataset produced by ISRIC—World Soil Information Center, which employs machine learning to predict soil attributes at six standard depths globally (250 × 250 m)[73].

Land cover data. To minimize anthropogenic and hydrological influences, we excluded croplands, urban areas, and water bodies using the MODIS MCD12C1 land cover product (Collection 6.1). A conservative masking strategy was applied: any pixel classified as cropland, urban, or water in any year from 2001 to 2021 was excluded from analysis.

To reduce disturbance-related uncertainty, we masked areas with frequent or severe burning using the MOSEV global burn severity product[74]. We calculated the maximum dNBR for each January–June period (2001–2021), then excluded pixels with a multi-year mean dNBR >660, effectively removing ~10.4% of the study area from greenness sensitivity analysis (Supplementary Fig. 15).

Permafrost regions and types were delineated using the Circum-Arctic Map of Permafrost and Ground-Ice Conditions from the National Snow and Ice Data Center[75] (NSIDC), which classifies permafrost based on extent into four categories: continuous (90–100%),

discontinuous (50–90%), sporadic (10–50%), and isolated patches (0–10%) (Supplementary Fig. 1).

Vegetation types were defined according to the Terrestrial Ecoregions of the World (TEOW) framework, which classifies global land areas into 14 biomes and 846 ecoregions (Supplementary Table 3). For our analysis, we focused on stable plant functional types (e.g., tundra, shrublands, grasslands) to assess long-term responses at the biome level.

Estimation of β_{SOT}

To quantify the sensitivity of spring greenness to the timing of permafrost thaw (β_{SOT}) and its temporal evolution, we applied a moving-window regression approach[68]. Given the 40-year satellite record, a 15-year sliding window was selected to balance sample size and temporal resolution, with sensitivity tests using 13- and 17-year windows confirming robustness (Supplementary Fig. 7). Within each window, β_{SOT} was estimated using three complementary approaches (Supplementary Fig. 4):

Ridge regression. To address multicollinearity among driving variables, including SOT and climate variables, we employed ridge regression[76,77] as the primary method for all main-text analyses. This regularization technique penalizes coefficient magnitude to reduce variance inflation, ensuring more stable estimates. In each window, the normalized anomalies of spring greenness indicators (GIs: kNDVI, SIF and GPP) were regressed against SOT, spring mean temperature (Temp), precipitation (prec), shortwave radiation (Srad), and atmospheric CO_2 concentration (CO_2):

$$GI_{anl} = C_0 \times SOT_{anl} + C_1 \times Temp_{anl} + C_2 \times Prec_{anl} + C_3 \times Srad_{anl} + C_4 \times CO2_{anl} + RES \quad (2)$$

Here, "anl" indicates the anomaly (i.e., deviation from the long-term mean), which removes the effects of background values while preserving interannual variations influencing vegetation growth[78]. C_0-C_4 represent regression coefficients of each driving factor. RES is the residual.

For interpretability, SOT advancement was defined as positive, and thus β_{SOT} was computed as the negative of the SOT coefficient, standardized by the mean GI, to enable comparisons across indicators:

$$\beta_{SOT} = \frac{-C_0}{Mean(GI)} \quad (3)$$

Ordinary least squares regression. As a baseline, we also applied standard OLS regression[79] using the same explanatory variables as the ridge model. While OLS is more straightforward and interpretable, it does not account for variable collinearity, which may inflate variance or bias coefficients. OLS estimates, therefore, provide a reference point for evaluating the robustness of ridge-derived results (Supplementary Fig. 9).

Log–log regression. To assess potential nonlinear effects and reduce artifacts from linear assumptions[80,81], we further applied a log-log regression with SOT as the sole driving variable:

$$\log_{10}GI = C_0 \times \log_{10}SOT + RES \quad (4)$$

Accordingly, β_{SOT} was calculated as:

$$\beta_{SOT} = -C_0 \quad (5)$$

This approach provides an alternative view of the SOT-greenness relationship under multiplicative scaling and complements the multivariate regression analyses.

In summary, ridge regression was selected as the main method due to its robustness to collinearity, OLS served as a transparent baseline for comparison, and log–log regression offered insights into potential nonlinear scaling. Together, these approaches ensured that our estimates of β_{SOT} were not artifacts of a single statistical choice but reflected consistent patterns across methods (Supplementary Fig. 9).

Analyses

Trend analysis. To quantify long-term changes in the sensitivity of spring greenness to thaw timing, we calculated the trend of β_{SOT}, which is defined as the Theil–Sen slope of β_{SOT} estimates across moving windows from 1982 to 2021 (Supplementary Fig. 4), expressed in ‰ day^{-1} window^{-1}. This method provides a robust, median-based trend estimator less sensitive to outliers. The significance of the trend was assessed using the non-parametric Mann–Kendall test, with a significance level set at $P < 0.05$.

Spatial attribution analysis. To identify the key environmental factors controlling the spatial variation in β_{SOT} trends over 1982–2021, we employed an explainable machine learning framework combining Random Forest (RF) modeling and SHAP. The dependent variable was the β_{SOT} trend estimated from ridge regression, while environmental factors were grouped into five categories: permafrost, climate, hydrology, vegetation, and soil nutrition. The permafrost category included SOT, SOF, and ALT; climate factors comprised spring temperature, precipitation, shortwave radiation, snow depth, and winter Tmin; hydrological factors included soil moisture and runoff; vegetation factors covered GUD, POS, DFS, kNDVI, and canopy height; and soil nutrition was represented by SOC and soil nitrogen. For multi-year variables, both mean states and linear trends were included. Details of all variables are provided in Supplementary Table 1.

RF models were trained using these factors. As a data-driven machine learning algorithm, RF does not require statistical assumptions about explanatory variables or target variables, and it leverages large datasets to enhance stability[82]. While collinearity among variables does not affect the overall model performance of RF, it can influence variable importance rankings, as strongly collinear variables may mask each other's contributions, reducing interpretability[83]. To mitigate this issue, we calculated variance inflation factors (VIF) within each category and excluded variables with VIF ≥ 3, including soil moisture, spring Tmin, mean kNDVI, and mean GUD[84].

To interpret the RF results, we applied SHAP to isolate the marginal contributions of each environmental factor to the target variable. SHAP values, calculated as absolute weighted average marginal contributions, were used to rank variable importance and identify dominant factors influencing β_{SOT} trends[63,85]. The RF models were fitted using the "ranger" package[86], and SHAP values were extracted with the "treeshap" package[87] in R (version 4.3.1).

Mechanistic pathway analysis. To better understand how the timing of spring thaw modulates vegetation greenness, we developed a mechanistic framework grounded in ecohydrological and climatological theory. Previous studies have suggested that permafrost thawing may influence vegetation through multiple interacting processes. Earlier thawing alters the surface energy budget by reducing albedo, thereby increasing absorbed solar radiation and accelerating soil warming are generally favorable for early-season plant growth[26,28]. Thaw timing also affects the onset of vegetation activity; by advancing GUD, it may extend the growing season and enhance carbon assimilation in spring[16,88]. In addition, changes in thaw dynamics influence subsurface hydrology, potentially increasing root-zone soil moisture through enhanced infiltration and reduced surface runoff, thereby improving water availability during the early growth period[17,18]. Based on this process-level understanding, we hypothesized that the sensitivity of vegetation greenness to thaw timing (β_{SOT}) is regulated

through three interconnected pathways: energy balance, phenological timing, and water availability. To test this hypothesis, we employed a suite of complementary approaches.

To disentangle the potential mechanisms underlying β_{SOT} trends, we adopted a causal inference framework using CCM, which is a nonparametric approach for detecting causality in coupled nonlinear systems[89]. Unlike correlation-based methods, CCM tests whether the historical states of a putative cause can reconstruct the time series of an effect, thus enabling causal interpretation in complex ecological systems. This method has been increasingly applied in Earth system science to uncover feedbacks and interactions beyond statistical association[90]. In this study, CCM was implemented at two spatial scales: (1) Regional level: We calculated the spatial mean of β_{SOT}, albedo, GUD, and ΔSM within each moving window. CCM was then applied to the resulting time series (1982–2021) to detect overall causal linkages across the study region. (2) Pixel level: CCM was further conducted at each grid cell to obtain spatially explicit patterns of causality. For each CCM test, the predictive skill (ρ) was used to assess causality. A variable was deemed to causally influence β_{SOT} if ρ increased and converged with larger library size (L, or step length). To statistically confirm convergence, we calculated the Spearman correlation between ρ and L; a significantly positive correlation ($p < 0.05$) indicated a robust causal relationship. All input variables were processed as anomalies to remove long-term trends, and the time lag was set to zero to focus on contemporaneous causal effects.

We conducted pixel-wise partial correlation analysis to assess their intermediary roles in the SOT-kNDVI relationship, while controlling for the influence of climatic variables. This approach isolates the unique contribution of each intermediary variable by removing the effects of confounding factors[67,91]. To assess temporal shifts, the analysis was performed separately for 1982–2001 and 2002–2021. Statistical significance for partial correlations was determined at a threshold of $p < 0.05$.

We used SEM to quantify direct and indirect effects of SOT on spring greenness[92]. The analysis was conducted separately for 1982–2001 and 2002–2021 to assess temporal shifts in pathway strengths based on the three hypothesized pathways introduced above. All variables were first standardized to ensure comparability across regions and units. The models were implemented at the pixel level, where each grid cell was treated as an independent unit. For each pixel, a separate SEM was constructed using the time series of gridded variables, and maximum likelihood estimation was used to derive the standardized path coefficients. After pixel-wise model fitting, we computed the direct, indirect, and total effects by multiplying the standardized coefficients along each path. To characterize general patterns across permafrost regions, we then calculated the spatial average of the pixel-level coefficients and reported the aggregated results in Fig. 3G, H. Model validity at each pixel was assessed using standard SEM fit indices: the χ^2 test ($p > 0.05$), Comparative Fit Index (CFI > 0.9), Standardized Root Mean Square Residual (SRMR < 0.08), Goodness of Fit Index (GFI > 0.95), and Root Mean Square Error of Approximation (RMSEA < 0.08). A model was considered acceptable if at least three of five criteria were met[93]. All SEM analyses were performed using the "lavaan" package in R[94].

Uncertainty analysis. To assess the robustness of our estimated β_{SOT} trends, we conducted uncertainty analyses from both spatial and temporal perspectives.

Spatial subsampling analysis: To evaluate the robustness of β_{SOT} estimates within each time window, we performed a spatial bootstrap procedure across all 15-year moving windows. Specifically, for each window, we randomly sampled 30% (or 70%) of valid pixels from the study region and computed the spatial mean of β_{SOT}. This process was repeated 200 times per window to characterize the uncertainty associated with spatial heterogeneity. Distributions of the resulting estimates were summarized using boxplots to quantify spatial uncertainty. The consistent temporal pattern and narrow uncertainty ranges across iterations indicate that the observed β_{SOT} dynamics are not driven by specific pixel configurations (Supplementary Fig. 13).

Temporal subsampling analysis: To evaluate the influence of interannual sampling variability within each 15-year moving window, we implemented a temporal bootstrap approach. Specifically, for each window, we randomly selected 10 out of the 15 years (without replacement) and recalculated pixel-wise β_{SOT} using ridge regression. This process was repeated 10 times, producing 10 sets of β_{SOT} trend estimates across the 26 windows from 1982 to 2021. For each pixel, we computed the Theil–Sen slope of β_{SOT} over time in each replicate and summarized the results by calculating the mean and SD across replicates. The SD map quantifies the sensitivity of trend estimates to temporal sampling variability. The high consistency across replicates confirms the stability of β_{SOT} trends over time (Supplementary Fig. 14).

Together, these spatial and temporal uncertainty analyses provide a comprehensive evaluation of the robustness of our findings and support the reliability of the detected β_{SOT} patterns and trends.

Reporting summary

Further information on research design is available in the Nature Portfolio Reporting Summary linked to this article.

Data availability

All data used in this study are freely available from public repositories. Freeze-thaw state data are provided by FT-ESDR (https://nsidc.org/data/nsidc-0477/versions/5). Satellite-based greenness indicators include kNDVI (https://www.environment.snu.ac.kr/data/longterm-vi), LCSPP v3.2 (https://zenodo.org/records/14568024), BESS v2.0 GPP (https://www.environment.snu.ac.kr/bessv2), GOSIF, CSIF, and VODCA v2 (https://researchdata.tuwien.at/records/t74ty-tcx62). Meteorological data are available from TerraClimate (https://www.climatologylab.org/). Global monthly CO_2 records are available from NOAA. ERA5-Land datasets are available from Google Earth Engine and Copernicus Climate Data Store (https://cds.climate.copernicus.eu/). In situ surface temperature records are available from GTN-P (https://gtnp.arcticportal.org/). Active layer thickness data are provided by ESA. Soil organic carbon and nitrogen data are available from SoilGrids (https://www.isric.org/explore/soilgrids). Maximum root depth is available from EartH2Observe (http://www.earth2observe.eu/). Global canopy height data are available from ETH Global Canopy Height 2020 (https://code.earthengine.google.com/126c172d63e7ce780596c8d26f06d384). Land cover datasets include TEOW biomes (https://www.worldwildlife.org/publications/terrestrial-ecoregions-of-the-world), MODIS MCD12C1 IGBP (https://lpdaac.usgs.gov/), MOSEV dNBR (https://zenodo.org/records/4265209), and permafrost type data from NSIDC. Source data are provided with this paper.

Code availability

All data analyses were performed using R v.4.3.1. The codes used in this study are available at Zenodo [https://doi.org/10.5281/zenodo.17543943][95].

References

1. Heijmans, M. M. P. D. Tundra vegetation change and impacts on permafrost. *Nat. Rev. Earth Environ.* **3**, 68–84 (2022).
2. Myneni, R. B., Keeling, C. D., Tucker, C. J., Asrar, G. & Nemani, R. R. Increased plant growth in the northern high latitudes from 1981 to 1991. *Nature* **386**, 698–702 (1997).
3. Zhu, Z. et al. Greening of the Earth and its drivers. *Nat. Clim. Change* **6**, 791–795 (2016).
4. Pearson, R. G. et al. Shifts in Arctic vegetation and associated feedbacks under climate change. *Nat. Clim. Change* **3**, 673–677 (2013).

5. Piao, S. et al. Characteristics, drivers and feedbacks of global greening. *Nat. Rev. Earth Environ.* **1**, 14–27 (2020).
6. Xu, X., Riley, W. J., Koven, C. D., Jia, G. & Zhang, X. Earlier leaf-out warms air in the north. *Nat. Clim. Change* **10**, 370–375 (2020).
7. Schuur, E. A. G. et al. Climate change and the permafrost carbon feedback. *Nature* **520**, 171–179 (2015).
8. Walvoord, M. A. & Kurylyk, B. L. Hydrologic impacts of thawing permafrost—a review. *Vadose Zone J.* **15**, 1–20 (2016).
9. Webb, E. E. et al. Permafrost thaw drives surface water decline across lake-rich regions of the Arctic. *Nat. Clim. Change* **12**, 841–846 (2022).
10. Biskaborn, B. K. et al. Permafrost is warming at a global scale. *Nat. Commun.* **10**, 264 (2019).
11. Smith, S. L., O'Neill, H. B., Isaksen, K., Noetzli, J. & Romanovsky, V. E. The changing thermal state of permafrost. *Nat. Rev. Earth Environ.* **3**, 10–23 (2022).
12. Natali, S. M., Schuur, E. A. G. & Rubin, R. L. Increased plant productivity in Alaskan tundra as a result of experimental warming of soil and permafrost. *J. Ecol.* **100**, 488–498 (2012).
13. Schuur, E. A. G. & Mack, M. C. Ecological response to permafrost Thaw and consequences for local and global ecosystem services. *Annu. Rev. Ecol. Evol. Syst.* **49**, 279–301 (2018).
14. Luo, S., Wang, J., Pomeroy, J. W. & Lyu, S. Freeze–Thaw changes of seasonally frozen ground on the Tibetan Plateau from 1960 to 2014. *J. Clim.* **33**, 9427–9446 (2020).
15. Li, X., Jin, R., Pan, X., Zhang, T. & Guo, J. Changes in the near-surface soil freeze–thaw cycle on the Qinghai-Tibetan Plateau. *Int. J. Appl. Earth Observ. Geoinf.* **17**, 33–42 (2012).
16. Wang, J. & Liu, D. Vegetation green-up date is more sensitive to permafrost degradation than climate change in spring across the northern permafrost region. *Glob. Change Biol.* **28**, 1569–1582 (2022).
17. Jin, X.-Y. et al. Impacts of climate-induced permafrost degradation on vegetation: a review. *Adv. Clim. Change Res.* **12**, 29–47 (2021).
18. Wrona, F. J. et al. Transitions in Arctic ecosystems: Ecological implications of a changing hydrological regime. *JGR Biogeosci.* **121**, 650–674 (2016).
19. Yang, M., Nelson, F. E., Shiklomanov, N. I., Guo, D. & Wan, G. Permafrost degradation and its environmental effects on the Tibetan Plateau: a review of recent research. *Earth-Sci. Rev.* **103**, 31–44 (2010).
20. Buermann, W. et al. Widespread seasonal compensation effects of spring warming on northern plant productivity. *Nature* **562**, 110–114 (2018).
21. Piao, S. et al. Evidence for a weakening relationship between interannual temperature variability and northern vegetation activity. *Nat. Commun.* **5**, 5018 (2014).
22. Jorgenson, M. T., Shur, Y. L. & Pullman, E. R. Abrupt increase in permafrost degradation in Arctic Alaska. *Geophys. Res. Lett.* **33**, 2005GL024960 (2006).
23. Berner, L. T. et al. Summer warming explains widespread but not uniform greening in the Arctic tundra biome. *Nat. Commun.* **11**, 4621 (2020).
24. Grünberg, I., Wilcox, E. J., Zwieback, S., Marsh, P. & Boike, J. Linking tundra vegetation, snow, soil temperature, and permafrost. *Biogeosciences* **17**, 4261–4279 (2020).
25. Miller, P. A. & Smith, B. Modelling tundra vegetation response to recent Arctic warming. *AMBIO* **41**, 281–291 (2012).
26. Tang, S. et al. Resonance between projected Tibetan Plateau surface darkening and Arctic climate change. *Sci. Bull.* **69**, 367–374 (2024).
27. Wang, J. & Liu, D. Deciphering the biophysical impact of permafrost greening on summer surface offset. *Earth's. Future* **12**, e2023EF004077 (2024).
28. Pistone, K., Eisenman, I. & Ramanathan, V. Observational determination of albedo decrease caused by vanishing Arctic sea ice. *Proc. Natl. Acad. Sci. USA* **111**, 3322–3326 (2014).
29. Dragoni, D. et al. Evidence of increased net ecosystem productivity associated with a longer vegetated season in a deciduous forest in south-central Indiana, USA. *Glob. Change Biol.* **17**, 886–897 (2011).
30. Richardson, A. D. et al. Influence of spring phenology on seasonal and annual carbon balance in two contrasting New England forests. *Tree Physiol.* **29**, 321–331 (2009).
31. Li, J. et al. Weakening warming on spring freeze–thaw cycle caused greening Earth's third pole. *Proc. Natl. Acad. Sci. USA* **121**, e2319581121 (2024).
32. Bui, M. T., Lu, J. & Nie, L. A review of hydrological models applied in the permafrost-dominated Arctic region. *Geosciences* **10**, 401 (2020).
33. Shu, S., Jain, A. K., Koven, C. D. & Mishra, U. Estimation of permafrost SOC stock and turnover time using a land surface model with vertical heterogeneity of permafrost soils. *Glob. Biogeochem. Cycles* **34**, e2020GB006585 (2020).
34. Wang, T. et al. Permafrost thawing puts the frozen carbon at risk over the Tibetan Plateau. *Sci. Adv.* **6**, eaaz3513 (2020).
35. Hjort, J. et al. Impacts of permafrost degradation on infrastructure. *Nat. Rev. Earth Environ.* **3**, 24–38 (2022).
36. Loranty, M. M. et al. Reviews and syntheses: changing ecosystem influences on soil thermal regimes in northern high-latitude permafrost regions. *Biogeosciences* **15**, 5287–5313 (2018).
37. Turetsky, M. R. et al. Permafrost collapse is accelerating carbon release. *Nature* **569**, 32–34 (2019).
38. Strauss, J. et al. Deep Yedoma permafrost: a synthesis of depositional characteristics and carbon vulnerability. *Earth-Sci. Rev.* **172**, 75–86 (2017).
39. Bintanja, R. & Andry, O. Towards a rain-dominated Arctic. *Nat. Clim. Change* **7**, 263–267 (2017).
40. Liljedahl, A. K. et al. Pan-Arctic ice-wedge degradation in warming permafrost and its influence on tundra hydrology. *Nat. Geosci.* **9**, 312–318 (2016).
41. Neumann, R. B. et al. Warming effects of spring rainfall increase methane emissions from thawing permafrost. *Geophys. Res. Lett.* **46**, 1393–1401 (2019).
42. Pilyugina, P. et al. A physics-informed machine learning framework for permafrost stability assessment. *IEEE Access* **13**, 96423–96433 (2025).
43. Kim, Y., Kimball, J. S., Glassy, J. & Du, J. An extended global Earth system data record on daily landscape freeze–thaw status determined from satellite passive microwave remote sensing. *Earth Syst. Sci. Data* **9**, 133–147 (2017).
44. Muñoz-Sabater, J. et al. ERA5-Land: a state-of-the-art global reanalysis dataset for land applications. *Earth Syst. Sci. Data* **13**, 4349–4383 (2021).
45. Chen, X. et al. Different responses of surface freeze and thaw phenology changes to warming among Arctic permafrost types. *Remote Sens. Environ.* **272**, 112956 (2022).
46. Kim, Y., Kimball, J. S., Zhang, K. & McDonald, K. C. Satellite detection of increasing Northern Hemisphere non-frozen seasons from 1979 to 2008: implications for regional vegetation growth. *Remote Sens. Environ.* **121**, 472–487 (2012).
47. Li, J., Wu, C., Peñuelas, J., Ran, Y. & Zhang, Y. The start of frozen dates over northern permafrost regions with the changing climate. *Glob. Change Biol.* **29**, 4556–4568 (2023).
48. Camps-Valls, G. et al. A unified vegetation index for quantifying the terrestrial biosphere. *Sci. Adv.* **7**, eabc7447 (2021).
49. Chen, J. M. et al. Vegetation structural change since 1981 significantly enhanced the terrestrial carbon sink. *Nat. Commun.* **10**, 4259 (2019).

50. Porcar-Castell, A. et al. Chlorophyll a fluorescence illuminates a path connecting plant molecular biology to Earth-system science. *Nat. Plants* **7**, 998–1009 (2021).
51. Hu, Z. et al. Decoupling of greenness and gross primary productivity as aridity decreases. *Remote Sens. Environ.* **279**, 113120 (2022).
52. Ding, Z., Peng, J., Qiu, S. & Zhao, Y. Nearly half of global vegetated area experienced inconsistent vegetation growth in terms of greenness, cover, and productivity. *Earth's. Future* **8**, e2020EF001618 (2020).
53. Jeong, S. et al. Persistent global greening over the last four decades using novel long-term vegetation index data with enhanced temporal consistency. *Remote Sens. Environ.* **311**, 114282 (2024).
54. Fang, J. et al. A long-term reconstruction of a global photosynthesis proxy over 1982–2023. *Sci. Data* **12**, 372 (2025).
55. Lian, X. et al. Diminishing carryover benefits of earlier spring vegetation growth. *Nat. Ecol. Evol.* **8**, 218–228 (2024).
56. Li, B. et al. BESSv2.0: A satellite-based and coupled-process model for quantifying long-term global land–atmosphere fluxes. *Remote Sens. Environ.* **295**, 113696 (2023).
57. Li, X. & Xiao, J. A global, 0.05-degree product of solar-induced chlorophyll fluorescence derived from OCO-2, MODIS, and reanalysis data. *Remote Sens.* **11**, 517 (2019).
58. Zhang, Y., Joiner, J., Alemohammad, S. H., Zhou, S. & Gentine, P. A global spatially contiguous solar-induced fluorescence (CSIF) dataset using neural networks. *Biogeosciences* **15**, 5779–5800 (2018).
59. Zotta, R.-M. et al. VODCA v2: multi-sensor, multi-frequency vegetation optical depth data for long-term canopy dynamics and biomass monitoring. *Earth Syst. Sci. Data* **16**, 4573–4617 (2024).
60. Friedlingstein, P. et al. Global Carbon Budget 2023. *Earth Syst. Sci. Data* **15**, 5301–5369 (2023).
61. Sitch, S. et al. Recent trends and drivers of regional sources and sinks of carbon dioxide. *Biogeosciences* **12**, 653–679 (2015).
62. Abatzoglou, J. T., Dobrowski, S. Z., Parks, S. A. & Hegewisch, K. C. TerraClimate, a high-resolution global dataset of monthly climate and climatic water balance from 1958–2015. *Sci. Data* **5**, 170191 (2018).
63. Li, W. et al. Widespread increasing vegetation sensitivity to soil moisture. *Nat. Commun.* **13**, 3959 (2022).
64. Pinzon, J. & Tucker, C. A non-stationary 1981–2012 AVHRR NDVI3g time series. *Remote Sens.* **6**, 6929–6960 (2014).
65. Shen, M. et al. Increasing altitudinal gradient of spring vegetation phenology during the last decade on the Qinghai–Tibetan Plateau. *Agric. For. Meteorol.* **189–190**, 71–80 (2014).
66. Chen, J. et al. A simple method for reconstructing a high-quality NDVI time-series data set based on the Savitzky–Golay filter. *Remote Sens. Environ.* **91**, 332–344 (2004).
67. Wang, J., Liu, D., Ciais, P. & Peñuelas, J. Decreasing rainfall frequency contributes to earlier leaf onset in northern ecosystems. *Nat. Clim. Change* **12**, 386–392 (2022).
68. Wu, C. et al. Increased drought effects on the phenology of autumn leaf senescence. *Nat. Clim. Change* https://doi.org/10.1038/s41558-022-01464-9 (2022).
69. Wang, X. & Wu, C. Estimating the peak of growing season (POS) of China's terrestrial ecosystems. *Agric. For. Meteorol.* **278**, 107639 (2019).
70. Fan, Y., Miguez-Macho, G., Jobbágy, E. G., Jackson, R. B. & Otero-Casal, C. Hydrologic regulation of plant rooting depth. *Proc. Natl. Acad. Sci. USA* **114**, 10572–10577 (2017).
71. Lang, N., Jetz, W., Schindler, K. & Wegner, J. D. A high-resolution canopy height model of the Earth. *Nat. Ecol. Evol.* **7**, 1778–1789 (2023).
72. Obu, J. et al. Northern Hemisphere permafrost map based on TTOP modelling for 2000–2016 at 1 km2 scale. *Earth-Sci. Rev.* **193**, 299–316 (2019).
73. Poggio, L. et al. SoilGrids 2.0: producing soil information for the globe with quantified spatial uncertainty. *Soil* **7**, 217–240 (2021).
74. Alonso-González, E. & Fernández-García, V. MOSEV: a global burn severity database from MODIS (2000–2020). *Earth Syst. Sci. Data* **13**, 1925–1938 (2021).
75. Brown, J., Ferrians, O., Heginbottom, J. A. & Melnikov, E. Circum-Arctic map of permafrost and ground-ice conditions. Version 2. 10.7265/skbg-kf16 (2002).
76. Chen, L. et al. Leaf senescence exhibits stronger climatic responses during warm than during cold autumns. *Nat. Clim. Change* **10**, 777–780 (2020).
77. He, L. et al. Lagged precipitation effects on plant production across terrestrial biomes. *Nat. Ecol. Evol.* https://doi.org/10.1038/s41559-025-02806-4 (2025).
78. Wang, S. et al. Recent global decline of CO_2 fertilization effects on vegetation photosynthesis. *Science* **370**, 1295–1300 (2020).
79. Fu, Y. H. et al. Declining global warming effects on the phenology of spring leaf unfolding. *Nature* **526**, 104–107 (2015).
80. Yang, G., Crowther, T. W., Lauber, T., Zohner, C. M. & Smith, G. R. A globally consistent negative effect of edge on aboveground forest biomass. *Nat. Ecol. Evol.* https://doi.org/10.1038/s41559-025-02840-2 (2025).
81. Wolkovich, E. M. et al. A simple explanation for declining temperature sensitivity with warming. *Glob. Change Biol.* **27**, 4947–4949 (2021).
82. Breiman, L. Random forests. *Mach. Learn.* **45**, 5–32 (2001).
83. Strobl, C., Boulesteix, A.-L., Kneib, T., Augustin, T. & Zeileis, A. Conditional variable importance for random forests. *BMC Bioinform.* **9**, 307 (2008).
84. Wang, X. et al. Enhanced habitat loss of the Himalayan endemic flora driven by warming-forced upslope tree expansion. *Nat. Ecol. Evol.* **6**, 890–899 (2022).
85. Berdugo, M., Gaitán, J. J., Delgado-Baquerizo, M., Crowther, T. W. & Dakos, V. Prevalence and drivers of abrupt vegetation shifts in global drylands. *Proc. Natl. Acad. Sci. USA* **119**, e2123393119 (2022).
86. Wright, M. N. & Ziegler, A. ranger: a fast implementation of random forests for high dimensional data in C++ and R. *J. Stat. Soft.* **77**, 1–17 (2017).
87. Lundberg, S. M. et al. From local explanations to global understanding with explainable AI for trees. *Nat. Mach. Intell.* **2**, 56–67 (2020).
88. Keenan, T. F. et al. Net carbon uptake has increased through warming-induced changes in temperate forest phenology. *Nat. Clim. Change* **4**, 598–604 (2014).
89. Sugihara, G. et al. Detecting causality in complex ecosystems. *Science* **338**, 496–500 (2012).
90. Shen, M. et al. Can changes in autumn phenology facilitate earlier green-up date of northern vegetation?. *Agric. For. Meteorol.* **291**, 108077 (2020).
91. Wu, C. et al. Contrasting responses of autumn-leaf senescence to daytime and night-time warming. *Nat. Clim. Change* **8**, 1092–1096 (2018).
92. Bagozzi, R. P. & Yi, Y. Specification, evaluation, and interpretation of structural equation models. *J. Acad. Mark. Sci.* **40**, 8–34 (2012).
93. Gao, S. et al. An earlier start of the thermal growing season enhances tree growth in cold humid areas but not in dry areas. *Nat. Ecol. Evol.* **6**, 397–404 (2022).
94. Rosseel, Y. lavaan: an R package for structural equation modeling. *J. Stat. Soft.* **48**, 1–36 (2012).
95. Hua, H., Wang, J. & Wu, C. Accelerated land surface greening caused by earlier permafrost thawing. Zenodo 10.5281/ZENODO.17543942 (2025).

Acknowledgements

This work was funded by the National Natural Science Foundation of China (42125101, W2412014). J.W. was funded by the National Natural

Science Foundation of China (42571037) and "Kezhen and Bingwei" Young Scientist Program of IGSNRR. C.M.Z. was funded by SNF Ambizione grant PZ00P3_193646. J.P. was funded by the TED2021-132627B-I00 grant funded by the Spanish MCIN, AEI/10.13039/501100011033 and by the European Union NextGenerationEU/PRTR, the Fundación Ramón Areces project CIVP20A6621 and the Catalan government grants SGR221-1333 and AGAUR2023 CLIMA 00118. We also appreciate the funding from the Science and Technology Program of Guangdong (No. 2024B1212070012).

Author contributions

C.W. designed the research. H.H. and J.W. wrote the first draft of the manuscript and performed the analyses. C.M.Z. and J.P. discussed the research design, interpretation, and manuscript revision. Y.R. provided methodological support. All authors assessed the analyses and contributed to improving the manuscript.

Competing interests

The authors declare no competing interests.

Additional information

Supplementary information The online version contains supplementary material available at https://doi.org/10.1038/s41467-025-67644-1.

Correspondence and requests for materials should be addressed to Chaoyang Wu.

Peer review information *Nature Communications* thanks Andreas Dietz, who co-reviewed with Martina WenzlSteven Cumming, and Tingting Xu for their contribution to the peer review of this work. A peer review file is available.